IEEE Photonics Journal
An IEEE Photonics Society Publication

Open Access

Accurate Modeling and Design of Graded-Index Fiber Probes for Optical Coherence Tomography Using the Beam Propagation Method

Volume 5, Number 2, April 2013

D. Lorenser
X. Yang
D. D. Sampson, Member, IEEE

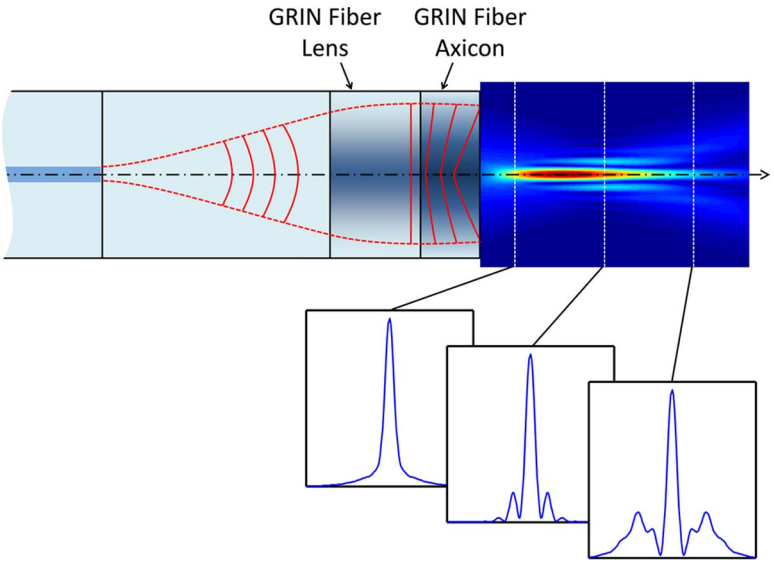

DOI: 10.1109/JPHOT.2013.2250939
1943-0655/$31.00 ©2013 IEEE

IEEE photonics SOCIETY

IEEE

Accurate Modeling and Design of Graded-Index Fiber Probes for Optical Coherence Tomography Using the Beam Propagation Method

D. Lorenser,[1] X. Yang,[1] and D. D. Sampson,[1,2] *Member, IEEE*

[1]Optical + Biomedical Engineering Laboratory, School of Electrical, Electronic and Computer Engineering, The University of Western Australia, Perth, WA 6009, Australia
[2]Centre for Microscopy, Characterisation and Analysis, The University of Western Australia, Perth, WA 6009, Australia

DOI: 10.1109/JPHOT.2013.2250939
1943-0655/$31.00 ©2013 IEEE

Manuscript received January 17, 2013; revised February 18, 2013; accepted February 20, 2013. Date of publication March 7, 2013; date of current version March 22, 2013. Corresponding author: D. Lorenser (e-mail: dirk.lorenser@uwa.edu.au).

Abstract: Fiber-optic probes for sensing and biomedical imaging applications such as optical coherence tomography (OCT) frequently employ sections of graded-index (GRIN) fiber to re-focus the diverging light from the delivery fiber. Such GRIN fiber microlenses often possess aberrations that cause significant distortions of the focused output beam. Current design methods based on ABCD matrix transformations of Gaussian beams cannot model such effects and are therefore inadequate for the analysis and design of high-performance probes that require diffraction-limited output beams. We demonstrate use of the beam propagation method (BPM) to analyze beam distortion in GRIN-lensed fibers resulting from index profiles that exhibit a deviation from the ideal parabolic shape or artifacts such as ripples or a central dip. Furthermore, we demonstrate the power of this method for exploring novel probe designs that incorporate GRIN phase masks to generate wavefront-shaped output beams with extended depth-of-focus (DOF). We present results using our method that are in good agreement with experimental data. The BPM enables accurate simulation of fiber probes using non-ideal or custom-engineered GRIN fibers with arbitrary refractive index profiles, which is important in the design of high-performance fiber-based micro-imaging systems for biomedical applications.

Index Terms: Biomedical optical imaging, optical microscopy.

1. Introduction

Miniaturized fiber-optic probes that can be delivered to deep-tissue locations via hypodermic needles or catheters are an enabling technology that allows minimally invasive optical biomedical imaging far beyond the normal depth penetration of light into biological tissues using techniques such as optical coherence tomography (OCT) [1]–[3]. Fig. 1(a) shows a schematic of a fiber-optic OCT imaging probe, consisting of an assembly of a single-mode fiber (SMF) terminated with focusing optics and a side-deflecting micromirror inside a hypodermic needle with a side opening, allowing the generation of 3-D images by rotation and pullback of the needle after its insertion into the tissue region of interest [4]. In order to eliminate the need for alignment of discrete micro-optical components, there has been a trend toward all-fiber probe designs using no-core fiber (NCF) spacers for beam expansion and sections of graded-index (GRIN) fiber that act as microlenses to focus the beam into the biological tissue for imaging at high resolution [2], [5]–[7]. Such highly

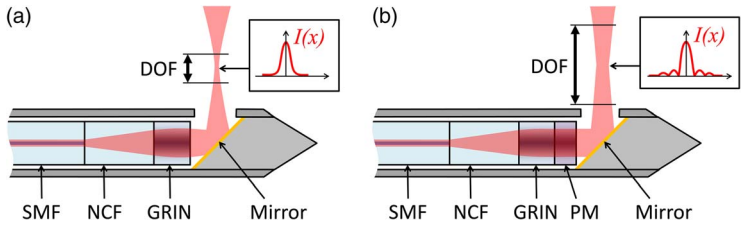

Fig. 1. (a) Schematic of a fiber-optic OCT needle probe. The focused output beam has a Gaussian transverse intensity profile. SMF, single-mode fiber; NCF, no-core fiber; GRIN, graded-index fiber; DOF, depth-of-focus. (b) Schematic of the same imaging probe as in (a), but with an additional GRIN phase mask (PM), which generates an output beam with a non-Gaussian transverse intensity profile that has similar transverse resolution but extended DOF compared to (a).

miniaturized all-fiber probes are amenable to fabrication using established fusion-splicing technology, which is reproducible and self-aligning, and which also ensures minimal losses and back reflections. Furthermore, we have recently shown that this all-fiber probe concept includes the possibility of adding a GRIN phase mask section after the GRIN lens section in order to generate a wavefront-shaped output beam with extended depth-of-focus (DOF) [8], as illustrated in Fig. 1(b).

For high-performance OCT imaging, it is important that the probe optics introduces minimal aberrations since the characteristics of the output beam determine the transverse resolution and also directly impact on the sensitivity of the system (as the signal level obtained from a point-like scattering object will depend on the peak intensity of the focused probe beam). One of the current limitations of fiber-optic OCT probes lies in the optical quality of the GRIN fiber lenses, as the probe designer is typically forced to choose from a finite range of commercially available multimode fibers (MMFs), which are optimized for optical telecommunications rather than for imaging. It was already recognized in early work that the refractive index profiles of such GRIN MMFs can exhibit significant deviations from the parabolic shape required for them to act as ideal GRIN lenses, which results in aberrations and sub-optimal optical performance [5], [9]. Improved preform fabrication methods [5], [10] have led to a new generation of high-bandwidth GRIN MMFs with smooth refractive index profiles, which are free of the central index dip that plagues legacy GRIN MMFs. However, these modern high-bandwidth GRIN MMFs are only available with small core diameters of 50 and 62.5 μm, limiting their use to probe designs with relatively low numerical aperture (NA) and working distance (WD). Furthermore, their index profiles tend to exhibit a more or less pronounced deviation from the ideal parabolic shape that is purposely introduced by the manufacturer in order to minimize intermodal pulse broadening in the targeted operating wavelength band [11], [12]. Thus, large-core-diameter fibers drawn from preforms of such high-bandwidth GRIN MMFs [5] will not necessarily behave as ideal GRIN lenses.

The aberrations introduced by index profiles with non-parabolic shapes and central dips cannot be modeled by current design methods based on ABCD matrix transformations of Gaussian beams [13], as these assume a perfect square-law refractive index profile of the GRIN fiber. ABCD matrix modeling has proven to be a useful framework for basic probe design and analysis [2], [6], [7], [14], [15] and as a simple tool for calculating approximate values for the GRIN fiber and NCF spacer section lengths, which can then be experimentally optimized to yield the desired output beam characteristics [7]. However, for the development of next-generation, high-performance OCT fiber probes, a more sophisticated numerical modeling technique is required for two reasons. First, in order to achieve diffraction-limited resolution and maximum sensitivity, it is necessary to quantify how imperfections of the GRIN fiber profile influence the beam quality and focal spot intensity (Strehl ratio), particularly in probe designs with high NA or long WD that may require the use of large-core-diameter GRIN fibers of sub-optimal quality. Second, the development of novel probe designs of the type shown in Fig. 1(b), which make use of GRIN fiber phase masks to generate non-Gaussian, wavefront-shaped output beams with increased DOF, requires a rigorous diffraction modeling method that can accommodate GRIN elements with arbitrary refractive index profiles.

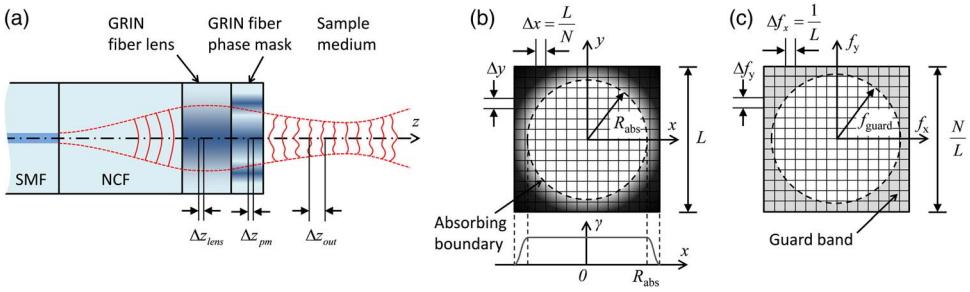

Fig. 2. (a) Schematic of our BPM simulation geometry. (b) The $N \times N$ simulation grid with dimension L sampled with increments $\Delta x = \Delta y = L/N$ and with an absorbing boundary of radius R_{abs}. (c) The $N \times N$ simulation grid in the spatial frequency domain sampled with increments $\Delta f_x = \Delta f_y = 1/L$ with a guard band of radius f_{guard}.

In this paper, we demonstrate the application of advanced numerical modeling based on the beam propagation method (BPM) [16], [17] to fiber-optic probes using GRIN lenses and phase masks. The BPM can be used to simulate light propagation through GRIN fibers with arbitrary refractive index profiles and to calculate the true 3-D diffracted field in the focal region of the probe, from which the designer can extract a wealth of advanced performance metrics beyond a rudimentary characterization in terms of WD and "spot size," including Strehl ratio and DOF.

One of the great strengths of the BPM is its validity for systems of arbitrary Fresnel numbers. (The Fresnel number $N = a^2/(\lambda L)$ determines whether the imaging system operates in the "near field" or in the "far field" of the diffraction pattern generated by the system aperture of radius a, where L is the distance of the focal region from the aperture, and λ is the wavelength [18].) Miniaturized fiber-optic probes for OCT are near-field systems with Fresnel numbers on the order of unity, and for this reason, it is difficult to extend their DOF by a straightforward application of schemes developed for bulk-optic microscopes (e.g., pupil plane phase masks [19] or axicons [20], [21]) since these are all derived under the assumption of large Fresnel number. Thus, the BPM is a necessary tool for studying schemes for creating focal regions with extended DOF in low-Fresnel-number systems such as fiber-optic probes.

The remainder of this paper is divided into three main sections. In Section 2, we describe our implementation of the BPM algorithm and its application to the problem of GRIN fiber probes, including a brief discussion of its numerical accuracy. In Section 3, we use the BPM to analyze beam distortions resulting from index profile aberrations that are common in commercial GRIN fibers, and we demonstrate good agreement with experimental data. In Section 4, we explore the performance of a novel probe design incorporating an axicon-like GRIN phase mask to generate a Bessel-like output beam with extended DOF.

2. Numerical Modeling Technique

The general simulation geometry used in this paper is illustrated in Fig. 2(a) [22]. The launched fundamental mode from the SMF is treated as an ideal Gaussian beam with a $1/e^2$ waist diameter equal to the mode field diameter (MFD) of the SMF, and its complex field amplitude at the location of the NCF/GRIN interface is used as the input to the BPM simulation. In the GRIN fiber lens, in the (optional) GRIN fiber phase mask, and in the sample medium, the field is numerically propagated with BPM step sizes Δz_{lens}, Δz_{pm}, and Δz_{out}, respectively (the step sizes are not necessarily identical as the BPM accuracy constraints differ in the various sections, as will be explained in Section 2.3). The field is sampled on a $N \times N$ Cartesian grid of dimension L, as illustrated in Fig. 2(b). As the BPM algorithm switches back and forth between the spatial and spectral (spatial-frequency) domains, the field is also represented by its discrete Fourier transform on a $N \times N$ spectral grid of dimension N/L, as shown in in Fig. 2(c). In order to prevent the sampled wave amplitude from exceeding the boundaries of the spatial and spectral grid during the numerical propagation, we have implemented two simple but effective measures. First, we apply an "absorbing boundary" (a 2-D window function) to the field amplitude in the spatial domain at every

BPM step in order to prevent large-angle diffracted light from reaching the edges of the grid and causing artifacts in the fast Fourier transform (FFT) [see Fig. 2(b)]. We have chosen a Tukey window, which smoothly tapers to zero at the grid boundary for radii exceeding a radius R_{abs}, which is chosen to lie within the cladding region of the fiber. During the simulation, we monitor the integrated beam power and can therefore detect when a significant amount of light reaches the boundary. Second, in the spectral domain, we define a "guard band," which covers all spatial frequencies that exceed a frequency of f_{guard}, which we choose to be 90% of the spectral grid half-width $N/2L$. At every BPM step, we compute the relative integrated spectral power in the guard band to check that it remains negligible (below 10^{-6} in the examples discussed in this paper).

We closely follow the implementation of the BPM in [17]; therefore, we review it only briefly here with a view toward some aspects that are important for its application to light propagation in GRIN fiber lenses and phase masks. Our BPM code is implemented in MATLAB, and the simulations presented in this paper took between 8–16 s on a basic desktop computer with a 2.4-GHz CPU and 4 GB of memory.

2.1. Beam Propagation Method

The BPM is a numerical technique for solving the scalar Helmholtz equation in a weakly inhomogeneous medium with a spatially dependent refractive index $n(\mathbf{r})$ [16]:

$$(\nabla^2 + k^2)U = 0, \tag{1}$$

where $k = n(\mathbf{r})k_0$ is the spatially dependent propagation constant, with $k_0 = 2\pi/\lambda_0$ and λ_0 denoting the vacuum values of the propagation constant and wavelength, respectively. In optical fibers, the refractive index variation is on the order of a few percent, and therefore, the refractive index can be expressed as $n(\mathbf{r}) = \bar{n} + \delta n(x, y)$, where $\bar{n}$ is a constant background refractive index (e.g., the index of the silica cladding), and $\delta n(x, y)$ is a small transverse index variation. The complex scalar wave amplitude U can be written as $U(x, y, z) = A(x, y, z)\exp(-i\bar{k}z)$, where $\bar{k} = \bar{n}k_0$ is the propagation constant in the background medium. Note that in [17], it is not assumed that $A(x, y, z)$ is a slowly varying amplitude (although this assumption is often made in the BPM, leading to a simplified paraxial version). From (1), we can obtain a differential equation for the amplitude A, which is first order in the propagation coordinate z:

$$\frac{\partial A}{\partial z} = -i\left[\left(\nabla_\perp^2 + k^2\right)^{1/2} - \bar{k}\right]A \cong \left[\frac{-i\nabla_\perp^2}{\left(\nabla_\perp^2 + \bar{k}^2\right)^{1/2} + \bar{k}} - ik_0\delta n(x, y)\right]A = \left[\hat{D} + \hat{N}\right]A, \tag{2}$$

where $\nabla_\perp^2$ is the Laplacian in the transverse coordinates, $\hat{D}$ is the diffraction operator in a homogeneous medium with refractive index $\bar{n}$, and $\hat{N}$ is an operator that accounts for the inhomogeneity of the refractive index. A formal solution to (2) can be written as

$$A(x, y, z + \Delta z) = \exp\left[(\hat{D} + \hat{N})\Delta z\right]A(x, y, z) \cong \exp(\hat{D}\Delta z)\exp(\hat{N}\Delta z)A(x, y, z). \tag{3}$$

As $\hat{D}$ and $\hat{N}$ are noncommutating operators, the last approximate equality is only valid for small index variations and sufficiently small step sizes Δz [16]. However, it enables implementation of an intuitive numerical solution where the propagation in the inhomogeneous medium can be approximated by a repeated step-wise application of a phase screen $\exp(\hat{N}\Delta z) = \exp(-ik_0\delta n\Delta z)$ followed by free-space propagation in homogeneous material with the background refractive index $\bar{n}$. For computational efficiency, the free-space propagation operator $\hat{D}$ is applied in the spectral domain after performing a 2-D FFT of the field amplitude. The propagated field amplitude after a single step of size Δz is therefore

$$A(x, y, z + \Delta z) = \mathrm{FFT}^{-1}\left\{\exp\left[\frac{i\Delta z(k_x^2 + k_y^2)}{\left(\bar{k}^2 - k_x^2 - k_y^2\right)^{1/2} + \bar{k}}\right]\mathrm{FFT}[\exp(-ik_0\delta n\Delta z)A(x, y, z)]\right\}, \tag{4}$$

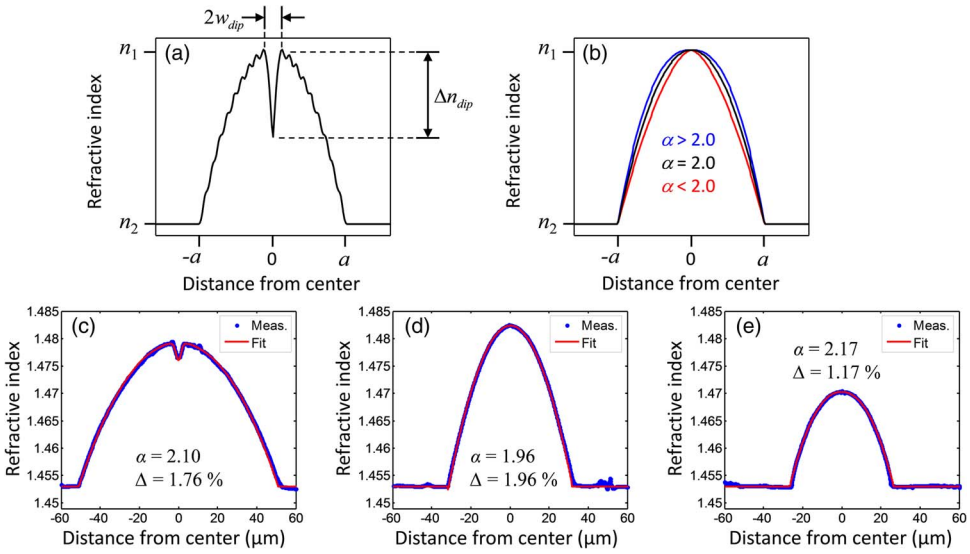

Fig. 3. (a) Power-law refractive index profile with central dip and ripple. (b) Illustration of the effect of the power-law exponent α on the profile shape. (c, d, e) Measured index profiles and power-law fits of several commercial fibers (the cladding index n_2 of all fibers is set to the refractive index $n = 1.453$ of pure silica at 800 nm). (c) 100-μm core-diameter GRIN MMF (100/140 MMF, POFC, Taiwan). (d) 62.5-μm core-diameter GRIN MMF (GIF625, Thorlabs, USA). (e) 50-μm core-diameter GRIN MMF (GIF50, Thorlabs, USA).

where $(k_x, k_y) = 2\pi(f_x, f_y)$ are the spatial frequency coordinates. As explained in [17], the spectral-domain diffraction operator in (4) is valid for high spatial frequencies, which is very important in this context because non-ideal index profiles may generate high spatial frequency components in the propagating field (e.g., due to the sharp central dip). Inspection of the square-root term in (4) shows that the diffraction operator approaches the paraxial (or Fresnel) diffraction operator $\exp(i\Delta z(k_x^2 + k_y^2)/2\bar{k})$ in the limit of small spatial frequencies $\sqrt{f_x^2 + f_y^2} \ll \bar{n}/\lambda_0$ and that it ensures exponential decay of sub-wavelength wavefront modulations with spatial frequencies that exceed the physical cutoff frequency $\bar{n}/\lambda_0$ of free-space propagation [23].

2.2. Refractive Index Profile Model

For the GRIN fiber lens, we use a power-law profile of the type widely used in the fiber-optic telecommunications literature, which has been modified to allow for the optional inclusion of a Gaussian central index dip or a sinusoidal "ripple" term [see Fig. 3(a)] [12]

$$n(r) = \begin{cases} n_1\left(1 - 2\Delta\left\{\left(\frac{r}{a}\right)^{\alpha} + h_{\text{dip}}\exp\left[-\left(\frac{r}{w_{\text{dip}}}\right)^2\right]\right\}\right)^{1/2} + h_{\text{rip}}\Delta n \sin\left(\frac{2\pi}{p_{\text{rip}}}r\right) & r < a \\ n_2 = n_1(1 - 2\Delta)^{1/2} & r \geq a, \end{cases} \quad (5)$$

where a is the core radius, and $\Delta = (n_1^2 - n_2^2)/2n_1^2$ is the relative index difference between the core and cladding refractive indices n_1 and n_2 (for small index differences, we can write $\Delta \cong \Delta n/n_1$, where $\Delta n = n_1 - n_2$). The central index dip is characterized by its relative depth $h_{\text{dip}} = \Delta n_{\text{dip}}/\Delta n$ and $1/e$-radius w_{dip}. The sinusoidal ripple is characterized by its relative amplitude $h_{\text{rip}} = \Delta n_{\text{rip}}/\Delta n$ and its period p_{rip}. The dip and ripple are index profile errors commonly encountered in GRIN fibers fabricated using the modified chemical vapor deposition (MCVD) method, where the dip results from "burnoff" of dopant during the high-temperature collapse of the preform, and the ripples result from the deposition of a finite number of layers of changing composition as well as gradients within these layers caused by dopant evaporation from the layer surface during vitrification [24]. The effect of the power-law exponent α on the profile shape is illustrated in Fig. 3(b).

Some example index profiles of commercial GRIN fibers, together with their best-fit power-law profiles, are shown in Fig. 3(c)–(e). Fig. 3(c) shows a 100-μm core-diameter GRIN MMF (100/140 MMF, POFC, Taiwan), which was profiled on an EXFO NR-9200 fiber analyzer at a wavelength of 655 nm. The fiber has an α-parameter of 2.1 and a central index dip with $w_{\text{dip}} = 1.8$ μm and $h_{\text{dip}} = 0.12$. This GRIN fiber produces significant beam distortion, as we will show in Section 3.3. Fig. 3(d) shows a 62.5-μm core-diameter GRIN MMF (GIF625, Thorlabs, USA), which we have used extensively in our recent work [2], [7] because probes fabricated using this fiber have exhibited very good Gaussian-like beam quality and shown fairly good agreement with ABCD matrix calculations. This observation is not surprising when one considers the index profile, which has no measurable dip in the center, and a near-parabolic shape with $\alpha = 1.96$. The 50-μm core-diameter GRIN MMF shown in Fig. 3(e) (GIF50, Thorlabs, USA) also has a very clean index profile with no central dip. However, its profile deviates markedly from the ideal parabolic shape with an α-parameter of 2.17, which is most likely due to its optimization for use with 850-nm lasers (Ge-doped GRIN fibers have optimum values of $\alpha > 2$ in the 850-nm telecommunications band [25]). The index profiles of GIF625 and GIF50 shown here were provided by the supplier (Thorlabs) and can be assumed to be representative of the characteristics of these particular products, but the reader should be aware that the profiles can vary slightly between manufacturing runs.

2.3. Numerical Accuracy of the BPM

In this section, we investigate the conditions that dictate the required sizes of the transverse sampling intervals $\Delta x = \Delta y$ of the computational grid and of the propagation increment Δz of the BPM. Due to the use of the discrete Fourier transform in the transverse dimensions, the Nyquist criterion applies, which requires that the transverse sampling interval must be smaller than half the period $p = 1/f_{\text{max}}$ of the highest spatial frequency component f_{max} of the propagating field, i.e.,

$$\Delta x < \frac{p}{2}. \tag{6}$$

We can estimate the value of f_{max} using the fiber NA, where $\text{NA} = \sqrt{n_1^2 - n_2^2} \cong n_1\sqrt{2\Delta}$. (This equation is normally derived for a step-index profile, but it can also be shown to hold true for GRIN fibers with a parabolic index profile.) The sine of the propagation angles of the angular spectrum will, therefore, be bounded by $\sin(\Theta_{\text{max}}) = \text{NA}/n_1$, which corresponds to a spatial frequency of $f_{\text{max}} = (\bar{n}/\lambda_0)\sin(\Theta_{\text{max}}) \cong \text{NA}/\lambda_0$. Therefore, we obtain the condition

$$\Delta x < \frac{\lambda_0}{2\text{NA}}. \tag{7}$$

Typical GRIN MMFs have NAs around 0.3 or less; therefore, we obtain a maximum sampling interval of $\sim 1.7\lambda_0$, which means we will have to sample on the scale of the wavelength. When simulating propagation in GRIN MMFs that have index profile features with very high spatial frequencies such as central index dips or high-frequency ripple, we need to re-examine the sampling requirements because the resulting wavefront modulations may result in angular spectral components that exceed the fiber NA. The Gaussian-shaped dip in our index profile model [see (5)] has a Gaussian spatial frequency spectrum that is approximately bounded by $f_{\text{max}} \cong 1/\pi w_{\text{dip}}$ (this is the $1/e^2$ radius of the power spectral density), and therefore, we obtain

$$\Delta x < \frac{\pi w_{\text{dip}}}{2}. \tag{8}$$

Consequently, this condition will take precedence over (7) when w_{dip} becomes smaller than the wavelength (however, the influence of the dip will start to diminish at this point because subwavelength wavefront modulations cannot propagate, as mentioned in Section 2.1).

The conditions that govern the choice of the BPM propagation step size Δz depend in a nontrivial way on the spatial-frequency content of the propagating wave as well as that of the inhomogeneous refractive index medium. A thorough analysis has been presented in [16], leading to a

set of five conditions [16, eqs. (41)–(43), (46), and (47)]. For our fiber NA and index profile model, we have found the most restrictive ones to be (46) and (47) (where we have used Θ_{max} instead of α to denote the upper bound of the angular spectrum, in order to avoid confusion with the power-law exponent), i.e.,

$$\Delta z \ll \frac{p}{\pi \tan(\Theta_{max})}, \text{ and} \tag{9}$$

$$\Delta z \ll \sqrt{\frac{p\,\lambda_0}{2\pi \tan(\Theta_{max})|\Delta n_{max}|}}. \tag{10}$$

The upper bound of the spatial frequency content of the propagating wave can again be estimated using the relation $\Theta_{max} \approx \sin^{-1}(NA/n_1)$. Let us first consider a power-law index profile with core radius a and no central index dip. The highest spatial frequencies of this index profile will have a period $p \approx a$. For a 0.3-NA, 50-μm core-diameter fiber at a wavelength of 800 nm, (10) turns out to be the most restrictive condition, with a maximum step size of $\Delta z = 23$ μm. If this fiber additionally has a central index dip of radius $w_{dip} = 1$ μm, then (9) becomes the most restrictive condition, yielding a maximum step size of $\Delta z = 5$ μm.

In practice, these numbers can be used as an orientation, and the optimum step size will become evident by running repeated simulations with decreasing Δz until the results converge to a steady state. Consistent with [16], we have found that the point of diminishing returns for decreasing Δz is of the same order as the limits calculated via (9) and (10). Therefore, in the context of the simulation tasks described in this work, there is no need to stay an order of magnitude below the calculated limits as the "$\ll$" in (9) and (10) might imply.

We have compared the results of our BPM code with ABCD matrix simulations of simple NCF/GRIN fiber probes with ideal parabolic refractive index profiles and found the relative errors of the values of focal spot diameter and WD to be less than 1%.

3. Analysis of Beam Distortions Caused by Index Profile Aberrations

In this section, we utilize our BPM code to analyze the effects of index profile variations from the ideal on the output beam of a lensed fiber probe. When we analyze distorted or wavefront-shaped output beams in the following, we will measure the "quality" of the focal region by two parameters that are of relevance to the performance of the probe for OCT imaging, namely, Strehl ratio and relative depth-of-focus (RDOF). The Strehl ratio of an aberrated system is defined as the ratio of its focal spot peak intensity to that of an equivalent diffraction-limited system [18]. Similarly, we define the RDOF as the ratio of the DOF of the simulated beam to that of an equivalent diffraction-limited system. In this context, we represent the equivalent diffraction-limited system by a suitably defined "reference" Gaussian beam. In the case of the weakly aberrated power-law profiles considered in this section, we define the reference Gaussian as the output beam produced by the corresponding aberration-free power-law profile with $\alpha = 2.0$ of infinite extent (not truncated at the core radius a, in order to eliminate aperture diffraction effects). For very strongly aberrated or wavefront-shaped systems, where an equivalent aberration-free system cannot be inferred in a straightforward manner, we define the reference Gaussian as the ideal Gaussian beam that has the same full-width at half-maximum (FWHM) focal spot diameter and integrated power as the simulated beam. We choose to use the FWHM rather than the more commonly used $1/e^2$ criterion because the former yields more meaningful values for the central lobe diameters of non-Gaussian output beams with sidelobes or pedestals, which often exceed relative levels of $1/e^2$.

Thus, the Strehl ratio is given by $S = \hat{I}/\hat{I}_{Gauss}$, with $\hat{I}$ denoting the peak intensity at the focus of the simulated beam, and $\hat{I}_{Gauss}$ the peak intensity of the reference Gaussian

$$\hat{I}_{Gauss} = \frac{2P}{\pi w_{Gauss}^2} = \frac{4\ln(2)P}{\pi d_{FWHM}^2} \tag{11}$$

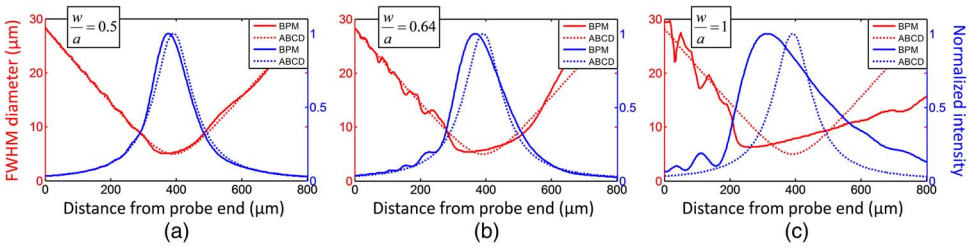

Fig. 4. BPM simulation results of a lensed fiber probe using a GRIN fiber lens with an ideal parabolic profile but finite core diameter, illustrating the effects of aperture diffraction on the output beam as a function of the fill factor w/a. The ABCD matrix simulation result for the case of an unbounded parabolic profile is shown for comparison (dotted curves). (a) Simulation of the example probe discussed in Section 3 with GRIN core radius $a = 50$ μm and fill factor of 0.5. (b), (c) Modified versions of the example probe, where the core radius a has been reduced to 39 (b) and 25 μm (c), increasing the fill factor to $2/\pi = 0.64$ and 1.0, respectively.

where P is the integrated beam power, w_{Gauss} is the $1/e^2$ waist radius of the reference Gaussian, and d_{FWHM} is the FWHM focal spot diameter of the simulated beam.

For calculation of the RDOF, we have chosen to define the DOF as the region over which the FWHM beam diameter is smaller than twice its minimum value (for the reference Gaussian, this yields a DOF that is $\sqrt{3}$ times larger than the Rayleigh-range DOF defined as $\text{DOF}_R = 2z_R$, where $z_R = n\pi w_{\text{Gauss}}^2/\lambda_0$, and n is the refractive index of the sample medium). Similar to our reasoning regarding the choice of FWHM beam diameters, this definition allows more tolerance for beam-width fluctuations in the focal region of non-Gaussian beam profiles than the Rayleigh-range criterion. We believe that this is justifiable because the Rayleigh range underestimates the perceived useful imaging depth range in OCT. (A 40% (factor of $\sqrt{2}$) change in transverse resolution is hardly visible in an OCT image due to the effects of logarithmic compression and speckle.)

Our example probe in this section is designed for high-resolution OCT imaging at a center wavelength of 800 nm with a FWHM transverse resolution of 5 μm. The probe design uses a 100-μm core-diameter GRIN MMF with $\Delta = 2\%$ and cladding index $n_2 = 1.453$ $(\text{NA} \approx 0.3)$, which is initially assumed to have a perfect parabolic profile with $\alpha = 2.0$ (or a gradient parameter of $g \cong \sqrt{2\Delta}/a = 4$ mm^{-1} in the equivalent ABCD matrix). The fundamental mode emitted from the SMF with a MFD of 5 μm is expanded in a 275-μm-long section of NCF so that its maximum $1/e^2$ beam radius w inside the GRIN fiber lens section equals half the core radius a. For a GRIN fiber length of 280 μm, an ABCD matrix simulation yields the desired output beam characteristics, with a $1/e^2$ focal spot diameter of 8.5 μm (FWHM diameter of 5 μm) at a WD of 390 μm (Fresnel number $N = 8$). This ideal Gaussian beam is used as the reference Gaussian in the examples discussed in the following subsections.

The BPM simulation of the probe using the aberration-free GRIN fiber with $\alpha = 2.0$ is consistent with the ABCD matrix result, but it reveals that the finite core diameter of the GRIN fiber results in some slight aperture diffraction effects on the beam, as shown in Fig. 4(a). (There is no measurable degradation of the beam quality, however, as the calculated Strehl ratio and RDOF are both still equal to 1.0.) We have intentionally chosen a relatively small fill factor $w/a = 0.5$ of the GRIN fiber core in order to minimize the influence of aperture diffraction on the beam profile as this would make the effects of the index profile aberrations that are introduced in the following subsections more difficult to interpret. To illustrate this point, we have also simulated our example probe with larger fill factors (obtained by reducing the core radius a of the GRIN fiber while keeping the gradient parameter g and the input beam parameters constant). The results are shown in Fig. 4(b) and (c), demonstrating that aperture diffraction starts to have a significant influence on the output beam profile even if only a small fraction of the total power in the beam is clipped. For example, if one uses a fill factor of $2/\pi = 0.64$ corresponding to the "aperture diameter $= \pi w$" rule [13] (this is the aperture size that transmits just over 99% of the Gaussian beam power), noticeable diffraction ripple and "focal shift" (a characteristic feature of focusing at low Fresnel numbers [26]) begin to appear, as can be seen in Fig. 4(b). Finally, for a fill factor of unity (86.4% of the Gaussian beam

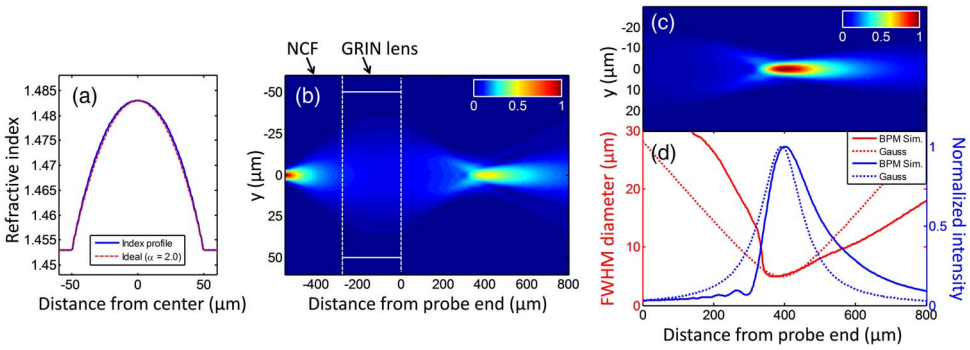

Fig. 5. BPM simulation of a GRIN-lensed fiber with $\alpha = 2.15$. (a) Index profile of the GRIN fiber compared to an ideal parabolic profile. (b) E-field amplitude in the entire simulated region. (c) Output beam intensity. (d) FWHM beam diameter and on-axis intensity of the simulated output beam (solid lines) compared to the reference Gaussian (dotted lines).

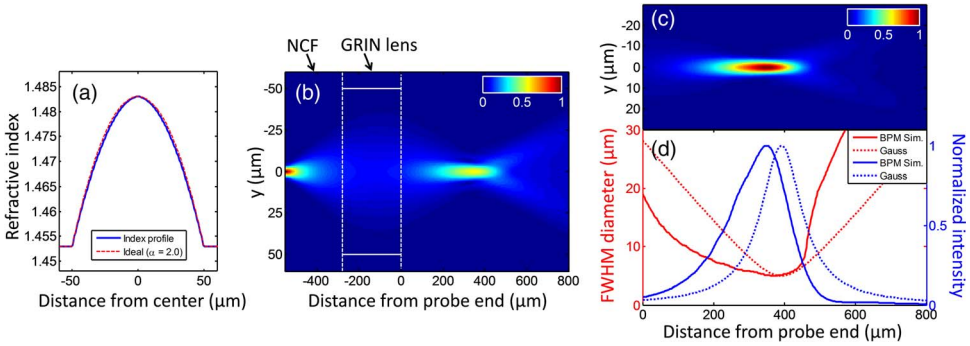

Fig. 6. BPM simulation of a GRIN-lensed fiber with $\alpha = 1.85$. (a) Index profile of the GRIN fiber compared to an ideal parabolic profile. (b) E-field amplitude in the entire simulated region. (c) Output beam intensity. (d) FWHM beam diameter and on-axis intensity of the simulated output beam (solid lines) compared to the reference Gaussian (dotted lines).

power passes the aperture), the ripple and the focal shift are so pronounced that the ABCD matrix simulation is no longer a useful approximation [see Fig. 4(c)]. These results highlight the limitations of the ABCD matrix approach for realistic modeling of fiber probes using GRIN fiber lenses, even for the case of aberration-free refractive index profiles.

In the BPM simulations presented in this section, we use a 256 $\times$ 256 grid with size $L = 150$ μm ($\Delta x = 0.59$ μm), and the background index $\bar{n}$ is set equal to the cladding index n_2.

3.1. Influence of the Power-Law Exponent

A deviation of the refractive index profile from the ideal parabolic shape in a GRIN lens is equivalent to spherical aberration (SA) in a refractive lens, with $\alpha > 2$ producing positive SA and $\alpha < 2$ producing negative SA. Figs. 5 and 6 show our BPM simulation results for the lensed fiber described above when we "de-tune" the power-law profile to values of $\alpha = 2.15$ and $\alpha = 1.85$, respectively, with all other parameters remaining unchanged (these values of α are representative of the maximum deviations from the ideal that one encounters in real GRIN MMFs). The BPM step size in the GRIN fiber is 2.4 μm. Figs. 5(d) and 6(d) show the FWHM beam diameters and on-axis intensities compared to the curves for the reference Gaussian. The on-axis intensities exhibit an asymmetric shape, which is characteristic of Gaussian beams focused with SA at low Fresnel numbers [27]. The de-tuning of α from the value of 2.0 does not just introduce SA, but it also changes the paraxial focusing power of the GRIN lens. These two effects shift the focal position in opposite directions, with the latter outweighing the former. Hence, there is a difference in the sign of

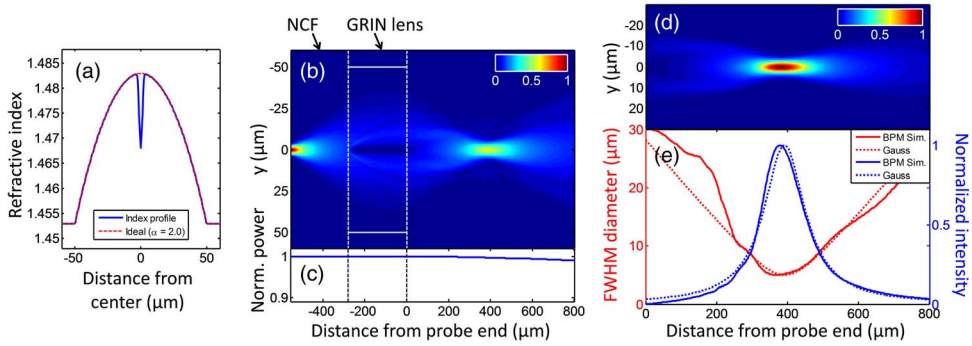

Fig. 7. BPM simulation of a GRIN-lensed fiber with $\alpha = 2.0$ and central index dip with $w_{\text{dip}} = 1.5$ μm and $h_{\text{dip}} = 0.5$. (a) Index profile of the GRIN fiber compared to an ideal parabolic profile. (b) E-field amplitude in the entire simulated region. (c) Normalized power of the propagating beam. (d) Output beam intensity. (e) FWHM beam diameter and on-axis intensity of the simulated output beam (solid lines) compared to the reference Gaussian (dotted lines).

our observed focal shift compared to [27] and other optics texts, where pure primary SA is added to an ideal lens of fixed focal length.

For the case of $\alpha = 2.15$, we obtain a significantly reduced Strehl ratio of $S = 0.77$ and a slight increase of the DOF $(\text{RDOF} = 1.1)$. In the case of $\alpha = 1.85$, the index profile begins to approach a triangular shape [see Fig. 6(a)], resulting in an axicon-like effect on the wavefront. As a result of this, the output beam starts to show features of a Bessel-like profile with sidelobes and an elongated focal region with RDOF $= 1.44$ obtained at the cost of a slightly reduced Strehl ratio of $S = 0.96$. We exploit this effect in Section 4 to design a GRIN phase mask with axicon-like properties in order to maximize the RDOF.

3.2. Influence of the Central Index Dip and Index Ripple

The effects of the central index dip and index ripple on the bandwidth of GRIN MMFs have been studied extensively in the fiber-optic telecommunications literature from the viewpoint of modal analysis [12], [24]. However, these studies provide little insight into the wavefront distortions that result when using short sections of such GRIN MMFs as lenses. Our aim here is to gain an intuitive understanding of the beam distortions resulting from central index dips and index ripples and to gauge the order of magnitude of their effect on the beam quality in terms of Strehl ratio and RDOF.

Fig. 7 shows the simulation of our example probe for $\alpha = 2.0$ and a central index dip with $h_{\text{dip}} = 0.5$ and $w_{\text{dip}} = 1.5$ μm. (These values are representative of such dips in measured profiles shown in the literature.) The BPM step size in the GRIN fiber is 1.2 μm. The index dip behaves as a strong localized negative lens that directs light away from the optical axis, producing a characteristic hole in the center of the output beam profile in the region immediately adjacent to the GRIN fiber end face, as can be seen in Fig. 7(b). We have indeed experimentally observed such "donut"-like output beams when using GRIN fibers with central index dips. Interestingly, the Strehl ratio and the DOF suffer only minimally, with $S = 0.97$ and RDOF $= 0.99$. This can be explained by considering that the input beam to the GRIN fiber has been expanded in the NCF section such that the index dip affects only a small fraction of the incident beam wavefront. The output beam can, therefore, be described as a superposition of two components. The first and main component is an aberration-free wavefront (with a small central "hole"), which has propagated in the outer regions of the core that are not affected by the central dip and which converges normally to form the focal region of the probe. The second component is a large-angle diffracted wave, which is generated near the beginning of the GRIN fiber and which cannot be refocused within the short (0.18-pitch) GRIN section. It therefore exits the GRIN fiber as a diverging wave, which interferes with the converging main component but rapidly diminishes in amplitude so that its effect on the focal region is negligible. Fig. 7(c) is a plot of the integrated beam power versus propagation distance, showing that the diverging wave generated by the dip begins to strike the absorbing boundary at a distance

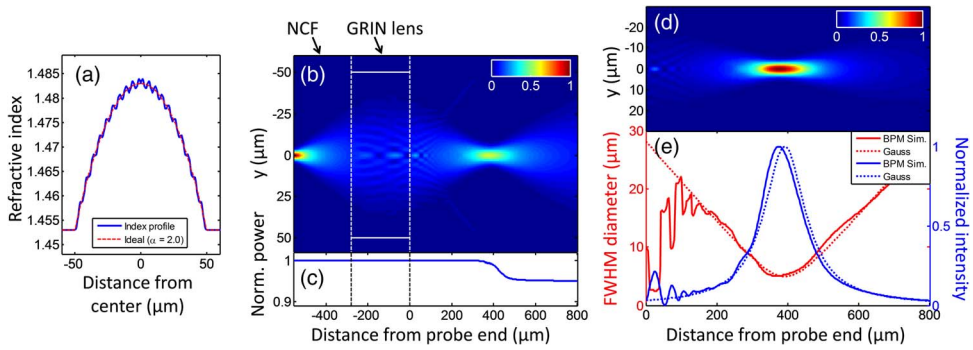

Fig. 8. BPM simulation of a GRIN-lensed fiber with $\alpha = 2.0$ and ripple with $h_{\text{rip}} = 0.03$ and $p_{\text{rip}} = 5$ μm. (a) Index profile of the GRIN fiber compared to an ideal parabolic profile. (b) E-field amplitude in the entire simulated region. (c) Normalized power of the propagating beam. (d) Output beam intensity. (e) FWHM beam diameter and on-axis intensity of the simulated output beam (solid lines) compared to the reference Gaussian (dotted lines). The sharp minima of the FWHM diameter curve near the probe end face should not be interpreted as intermediate foci because the FWHM is not a good measure of the transverse extent of the beam in the presence of strong modulations caused by interference.

of $\sim$300 μm from the probe and is gradually absorbed. When changing the dip parameters, it is not surprising that the width of the dip turns out to be most critical as it determines the fraction of the incident beam power that is intercepted by the dip. Doubling the dip radius to $w_{\text{dip}} = 3$ μm decreases the Strehl ratio to 0.88, whereas doubling the dip depth to $h_{\text{dip}} = 1$ only causes a minimal further reduction in the Strehl ratio to 0.96.

Next, we have investigated the effect of index ripple on the output beam. Our intuitive expectation is that, during every BPM step, the superimposed ripple behaves as a thin sinusoidal phase grating, which diffracts power out of the propagating beam at angles in the vicinity of $\Theta \approx \sin^{-1}[\lambda_0/(\bar{n}p_{\text{rip}})]$ [23]. This is confirmed by our simulations, as illustrated by the example shown in Fig. 8 for the case of our example probe, where the index profile with $\alpha = 2.0$ is modulated by ripple with $h_{\text{rip}} = 0.03$ (6% peak-to-peak) and $p_{\text{rip}} = 5$ μm. The BPM step size in the GRIN fiber is 1.2 μm. Fig. 8(b) shows that the output beam can again be interpreted as consisting of a superposition of an aberration-free and a large-angle diffracted component. The aberration-free component converges normally to an essentially un-altered focal spot with $S = 0.94$ and RDOF $= 0.98$, whereas the large-angle diffracted component diverges at the GRIN fiber end where it interferes with the aberration-free component but quickly propagates away from the optical axis. The plot of integrated beam power versus propagation distance in Fig. 8(c) shows that the large-angle diffracted component, which carries $\sim$5% of the beam power, strikes the absorbing boundary at a distance of $\sim$ 400 μm from the probe end. The amplitude of the ripple encountered in real fibers is typically lower than in this example. Therefore, our conclusion is that index ripple introduces negligible power loss (reducing the amplitude to $h_{\text{rip}} = 0.01$ restores the Strehl ratio to unity) and has practically no impact on the beam profile in the focal region. A more accurate modeling of the index ripple of real fibers would take into account that the typical spatial frequencies of the ripple are higher than shown in this example and that the ripple tends to be "chirped," increasing to very high spatial frequencies (submicron periodicity) near the edges of the profile [24]. However, this does not change our conclusion as higher spatial frequencies will simply diffract outward at even larger angles (and eventually become "invisible" to the wavefront when they exceed the physical cutoff frequency of $\bar{n}/\lambda_0$ of free-space propagation). When performing simulations for different ripple periods, we found that the most noticeable effects are caused by low-frequency ripple with only 1–3 periods in the core radius, as these produce beam distortions in the focal region of the probe and can cause degradation or enhancement of Strehl ratio and RDOF on the order of 10% even for very small amplitudes of 1% peak-to-peak. Even though such low-frequency ripple is not an inherent feature of the MCVD process, it can represent a systematic low-frequency deviation of the profile shape from the power-law model, which has indeed been observed in practical fibers [12].

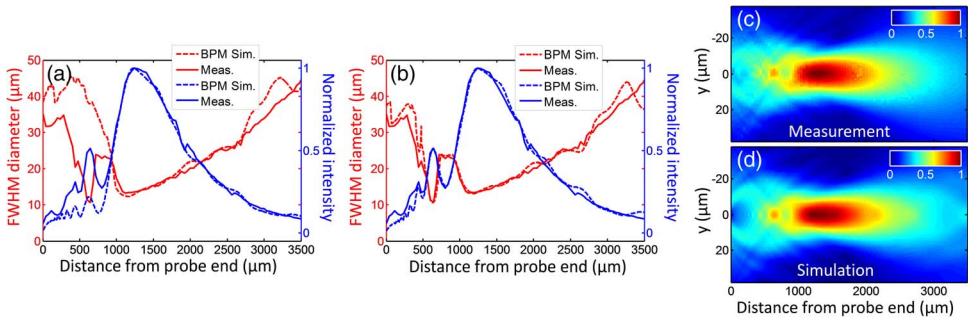

Fig. 9. Comparison of BPM simulation to the measured beam profile of a lensed fiber using the GRIN MMF with the index profile shown in Fig. 3(c). (a) Simulated vs. measured FWHM beam diameter and on-axis intensity, where the simulation uses the index profile fit shown in Fig. 3(c). (b) Same as (a), but with modified index profile including sinusoidal ripple (see text). (c) Measured output beam E-field amplitude (square root of measured intensity profile). (d) Simulated output beam E-field amplitude.

3.3. Comparison With Experimental Results

To demonstrate the accuracy of the BPM code, we have fabricated a lensed fiber using the 100/140 GRIN MMF with the measured index profile shown in Fig. 3(c), with lengths of 480 μm of NCF and 170 μm of GRIN fiber, which is spliced to SMF with a MFD of 5.6 μm at 830 nm (SM800, Fibercore, U.K.). The GRIN fiber used for this probe was from the same reel from which the sample for the index profile measurement was taken. The output beam was profiled as a function of distance from the probe at a wavelength of 820 nm using a commercial near-field beam profiler (SP620U, Ophir-Spiricon, USA). Fig. 9 shows the comparison of the simulation with the beam profiling results. The BPM step size in the GRIN fiber was 1.2 μm. Using the power-law index profile fit with central dip shown in Fig. 3(c), we are able to correctly model the beam diameter and on-axis intensity distribution in the focal region, as shown in Fig. 9(a). However, in the region immediately adjacent to the probe end face, there remains some disagreement between the simulated and measured curves. Based on the assumption that this is caused by subtle features of the index profile that are not correctly represented in our model, we have empirically found that adding a small amount of low-frequency sinusoidal ripple to the index profile in the BPM simulation reproduces the fine structure of the measured beam profile in this region with surprising fidelity, as shown in Fig. 9(b). The best agreement was obtained with $h_{\text{rip}} = 0.008$ and $p_{\text{rip}} = 35$ μm. Due to the very small relative amplitude of 1.6% peak-to-peak and the long period, this ripple is difficult to discern with the eye in the measured index profile of Fig. 3(c), but adding the ripple term to the fit curve reduces the RMS error of the fit from $8.2 \cdot 10^{-6}$ to $6.4 \cdot 10^{-6}$. The good overall agreement between the measured and simulated beam profile when using the rippled index profile is evident when comparing the plots of the E-field amplitude shown in Fig. 9(c) and (d). This result confirms our finding in Section 3.2 that even very small low-spatial-frequency deviations from the power-law shape on the order of 1% can have a noticeable effect on the output beams of lensed fibers.

The BPM simulation accurately predicts the WD and focal spot diameter of the probe. It yields a Strehl ratio of $S = 0.85$ and RDOF $= 1.0$, and it reveals the asymmetric intensity distribution of the focal region, which is due to the combined effects of positive SA resulting from the non-parabolic profile $(\alpha = 2.1)$ and aperture diffraction at the GRIN fiber core boundary (the fill factor in this design is $\sim$0.7). Furthermore, it predicts the characteristic "donut"-like transverse intensity profile at the end face of the GRIN fiber, which is caused by the central index dip.

4. Extending the DOF Using GRIN Fiber Phase Masks

Even when diffraction-limited focal regions can be achieved by using high-quality GRIN fibers, the straightforward lensed fiber probes with Gaussian output beams suffer from the problem of very low DOF at high transverse resolutions (as an example, for 5-μm FWHM transverse resolution, we have a DOF of only 246 μm in air or 344 μm in tissue with average refractive index $n = 1.4$ when using

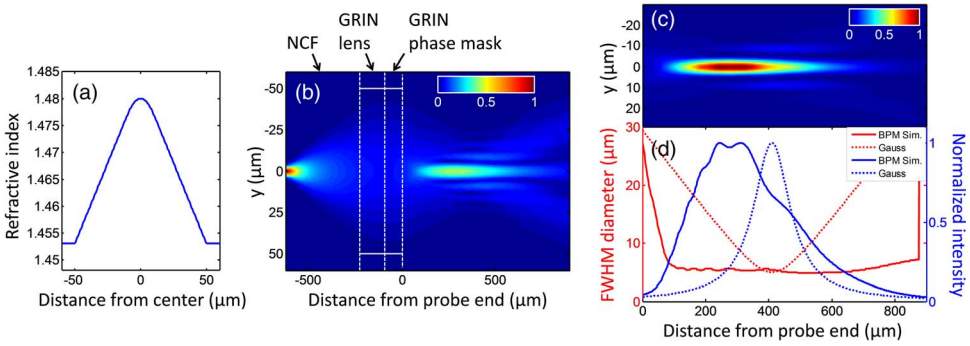

Fig. 10. BPM simulation of a GRIN fiber probe using a phase mask to increase the DOF. (a) Index profile of the axicon-like GRIN phase mask. (b) E-field amplitude in the entire simulated region. (c) Output beam intensity. (d) FWHM beam diameter and on-axis intensity of the simulated output beam (solid lines) and an ideal Gaussian beam with the same focal spot diameter (dotted lines). The apparent discontinuity of the FWHM diameter of the simulated beam (solid red line) near the end of the DOF is caused by the sidelobes of the beam, which begin to exceed 50% of the central lobe peak intensity beyond that point.

our DOF criterion of beam expansion to twice the focal spot diameter). We have recently demonstrated that the DOF of lensed fiber probes can be extended by a factor of ~2 using a simple phase mask consisting of a short section of overfilled GRIN MMF [8]. Here, we use our BPM code to explore the possibility of achieving even greater DOF gains by using a custom-designed axicon-like GRIN phase mask to generate a Bessel-like output beam. We begin our design with a standard lensed fiber for a wavelength of 800 nm using SMF with 5-μm MFD, a 400-μm-long NCF spacer, and a 135-μm-long section of 100-μm core-diameter GRIN MMF with $\alpha = 2.0$, $\Delta = 2\%$, and cladding index $n_2 = 1.453$. This spacer/lens combination produces a collimated beam with a $1/e^2$ diameter of 66 μm, which is used as the input to a 95-μm-long, 100-μm core-diameter GRIN fiber phase mask section with the index profile shown in Fig. 10(a). Such axicon-like GRIN fibers are not commercially available, but their production is feasible using existing preform fabrication techniques.

Identical BPM step sizes of 2.4 μm were used in the GRIN lens and GRIN phase mask sections. The plots of the simulated field amplitude and intensity in Fig. 10(b) and (c), respectively, show that the output beam of this probe exhibits the characteristic features of Bessel-like beams generated by low-Fresnel-number axicons [28], with a small number of sidelobes and an axial intensity distribution that is shifted toward the axicon. Fig. 10(d) shows that the FWHM diameter of the central lobe stays approximately constant around 5 μm over a large distance of ~800 μm in air, yielding a substantial DOF gain (RDOF ~ 3.3) compared to the reference Gaussian [dotted lines in Fig. 10(d)], which is obtained at the cost of a reduced Strehl ratio of $S = 0.56$. (The exact value of the useful DOF of this beam will be determined by the acceptable relative intensity of the sidelobes, which gradually increases to 50% of the central lobe intensity at the far end of the DOF.) The central lobe carries 36% of the total beam power in the middle of the Bessel-like region at ~400 μm from the probe end, which is significantly higher than in the case of bulk-optic axicons used at large Fresnel numbers in benchtop OCT systems, where the central lobe carries only a few percent of the total beam power [21]. A tolerance analysis of this probe design using the BPM showed that the Bessel-like structure of the focal region is quite robust against fabrication errors in the lengths of the NCF, GRIN, and phase mask sections. For well-calibrated splicing and cleaving setups, a repeatability of ± 5 μm can be achieved. The most sensitive lengths are those of the GRIN and phase mask sections, where errors of 5 μm cause changes in the central lobe diameter and DOF on the order of 10%; whereas, a variation of the NCF length by the same amount only causes changes in the output beam parameters of a few percent.

5. Conclusion

In summary, we have demonstrated the usefulness of the BPM for accurate modeling of GRIN fiber probes for future needle-based or micro-endoscopic OCT applications where optimum resolution

and sensitivity will be crucial for enabling minimally invasive imaging with quality comparable to state-of-the-art benchtop microscopes.

Our simulations have revealed a number of new insights about GRIN fiber lenses, which cannot be obtained using established ABCD matrix modeling techniques. The most significant finding is that low-spatial-frequency features of the index profile (such as deviation of the power-law exponent α from the ideal value of 2.0 or low-spatial-frequency variations of the profile about the power-law shape) are much more critical for the output beam quality than high-spatial-frequency features such as central index dips and short-period ripples, which are often encountered in fibers drawn from preforms fabricated using the MCVD process. This finding is important for specifying the fabrication tolerances of customized preforms for high-quality GRIN fiber lenses. It was also found that the negative SA introduced by profiles with $\alpha < 2.0$ can be used to enhance the DOF, whereas the positive SA introduced by values of $\alpha > 2.0$ produces less favorable output beam distortions that result in a significantly reduced Strehl ratio.

Furthermore, we have demonstrated the power of the BPM for studying advanced probe designs incorporating novel optical elements such as GRIN phase masks with arbitrary refractive index profiles to engineer the 3-D diffracted field in the focal region. We would like to point out that the BPM naturally also includes the possibility of multiplying the propagating wavefront with a "thin" phase or amplitude mask (which could, for example, represent a diffractive optical element created by microstructuring the fiber tip). The BPM has also successfully been used to model refractive surfaces such as waveguide lenses [29] and hemispherical lenses [8]. This capability is important for studying the effects of enclosing catheters, capillaries, or other transparent protective sheaths on the output beams of side-facing lensed fiber probes. (The analysis of astigmatism introduced by such cylindrical interfaces is obviously an important aspect of any realistic side-facing probe design, and it has been studied extensively using ABCD matrix simulations for the case of probes with Gaussian output beams [2], [7], [14], [15].)

In this paper, we have neglected wavefront distortions that the output beams incur as they propagate in biological tissue. However, the BPM can be used to study these effects if the tissue is modeled as an inhomogeneous dielectric medium, and such simulations have provided important insights regarding optimum beam shapes for microscopy in dense scattering media [30], [31].

In this paper, we have focused on GRIN fiber probes for OCT imaging, but the methods described here can also be applied to other imaging systems incorporating GRIN elements, such as microendoscopes for confocal fluorescence [32] or multiphoton microscopy [33], which use very thin fiber-like GRIN relay rods and lenses with diameters down to 350 μm at moderate NAs in the range 0.3–0.5, where scalar diffraction theory (which is the underlying framework of the BPM) is still very accurate. Some elements of the work presented here could also be useful for non-biomedical applications of GRIN fiber microlenses, such as analysis and design of fiber-to-freespace or fiber-to-fiber coupling assemblies in photonic devices and interconnects [9], [34].

References

[1] X. Li, C. Chudoba, T. Ko, C. Pitris, and J. G. Fujimoto, "Imaging needle for optical coherence tomography," *Opt. Lett.*, vol. 25, no. 20, pp. 1520–1522, Oct. 2000.

[2] D. Lorenser, X. Yang, R. W. Kirk, B. C. Quirk, R. A. McLaughlin, and D. D. Sampson, "Ultrathin side-viewing needle probe for optical coherence tomography," *Opt. Lett.*, vol. 36, no. 19, pp. 3894–3896, Oct. 2011.

[3] R. A. McLaughlin, B. C. Quirk, A. Curatolo, R. W. Kirk, L. Scolaro, D. Lorenser, P. D. Robbins, B. A. Wood, C. M. Saunders, and D. D. Sampson, "Imaging of breast cancer with optical coherence tomography needle probes: Feasibility and initial results," *IEEE J. Sel. Topics Quantum Electron.*, vol. 18, no. 3, pp. 1184–1191, May/Jun. 2012.

[4] B. C. Quirk, R. A. McLaughlin, A. Curatolo, R. W. Kirk, P. B. Noble, and D. D. Sampson, "In situ imaging of lung alveoli with an optical coherence tomography needle probe," *J. Biomed. Opt.*, vol. 16, no. 3, p. 036009, Mar. 2011.

[5] W. A. Reed, M. F. Yan, and M. J. Schnitzer, "Gradient-index fiber-optic microprobes for minimally invasive in vivo low-coherence interferometry," *Opt. Lett.*, vol. 27, no. 20, pp. 1794–1796, Oct. 2002.

[6] Y. Mao, S. Chang, S. Sherif, and C. Flueraru, "Graded-index fiber lens proposed for ultrasmall probes used in biomedical imaging," *Appl. Opt.*, vol. 46, no. 23, pp. 5887–5894, Aug. 2007.

[7] L. Scolaro, D. Lorenser, R. A. McLaughlin, B. C. Quirk, R. W. Kirk, and D. D. Sampson, "High-sensitivity anastigmatic imaging needle for optical coherence tomography," *Opt. Lett.*, vol. 37, no. 24, pp. 5247–5249, Dec. 2012.

[8] D. Lorenser, X. Yang, and D. D. Sampson, "Ultrathin fiber probes with extended depth of focus for optical coherence tomography," *Opt. Lett.*, vol. 37, no. 10, pp. 1616–1618, May 2012.
[9] W. Emkey and C. Jack, "Analysis and evaluation of graded-index fiber lenses," *J. Lightw. Technol.*, vol. LT-5, no. 9, pp. 1156–1164, Sep. 1987.
[10] D. Mazzarese, G. E. Oulundsen III, I. T. F. McMahon, and M. T. Owsiany, "Method of collapsing a tube for an optical fiber preform," U.S. Patent 6 718 800, Apr. 13, 2004.
[11] R. Olshansky and D. Keck, "Pulse broadening in graded-index optical fibers," *Appl. Opt.*, vol. 15, no. 2, pp. 483–491, Feb. 1976.
[12] D. Marcuse, "Calculation of bandwidth from index profiles of optical fibers. 1: Theory," *Appl. Opt.*, vol. 18, no. 12, pp. 2073–2080, Jun. 1979.
[13] A. E. Siegman, *Lasers*. Mill Valley, CA, USA: Univ. Sci. Books, 1986.
[14] W. Jung, W. A. Benalcazar, A. Ahmad, U. Sharma, H. Tu, and S. A. Boppart, "Numerical analysis of gradient index lens based optical coherence tomography imaging probes," *J. Biomed. Opt.*, vol. 15, no. 6, pp. 066027-1–066027-10, Nov./Dec. 2010.
[15] W. A. Benalcazar, W. Jung, and S. A. Boppart, "Aberration characterization for the optimal design of high-resolution endoscopic optical coherence tomography catheters," *Opt. Lett.*, vol. 37, no. 6, pp. 1100–1102, Mar. 2012.
[16] J. Van Roey, J. Van der Donk, and P. E. Lagasse, "Beam-propagation method: Analysis and assessment," *J. Opt. Soc. Amer.*, vol. 71, no. 7, pp. 803–810, Jul. 1981.
[17] M. D. Feit and J. A. Fleck, Jr., "Light propagation in graded-index optical fibers," *Appl. Opt.*, vol. 17, no. 24, pp. 3990–3998, Dec. 1978.
[18] M. Born and E. Wolf, *Principles of Optics*. Cambridge, U.K.: Cambridge Univ. Press, 1999.
[19] L. Liu, C. Liu, W. C. Howe, C. J. R. Sheppard, and N. Chen, "Binary-phase spatial filter for real-time swept-source optical coherence microscopy," *Opt. Lett.*, vol. 32, no. 16, pp. 2375–2377, Aug. 2007.
[20] Z. Ding, H. Ren, Y. Zhao, J. S. Nelson, and Z. Chen, "High-resolution optical coherence tomography over a large depth range with an axicon lens," *Opt. Lett.*, vol. 27, no. 4, pp. 243–245, Feb. 2002.
[21] R. A. Leitgeb, M. Villiger, A. H. Bachmann, L. Steinmann, and T. Lasser, "Extended focus depth for Fourier domain optical coherence microscopy," *Opt. Lett.*, vol. 31, no. 16, pp. 2450–2452, Aug. 2006.
[22] D. Lorenser, X. Yang, and D. D. Sampson, "Analysis of fiber-optic probes using graded-index fiber microlenses with non-ideal refractive index profiles," in *Proc. SPIE 22nd Int. Conf. Opt. Fiber Sens.*, vol. 8421, Y. Liao, H. Ho, D. D. Sampson, R. Yamauchi, Y. Chung, K. Nakamura, and Y. Rao, Eds., Bellingham, WA, USA, 2012, 84211W.
[23] J. Goodman, *Introduction to Fourier Optics*. New York, NY, USA: McGraw-Hill, 1968.
[24] A. Carnevale and U. C. Paek, "Empirical evaluation of profile variations in an MCVD optical waveguide fiber using modal structure analysis," *Bell Syst. Tech. J.*, vol. 62, no. 7, pp. 1937–1954, Sep. 1983.
[25] G. E. Peterson, A. Carnevale, U. C. Paek, and J. W. Fleming, "Numerical calculation of optimum alpha for a germania-doped silica lightguide," *Bell Syst. Tech. J.*, vol. 60, no. 4, pp. 455–470, Apr. 1981.
[26] Y. Li and E. Wolf, "Three-dimensional intensity distribution near the focus in systems of different Fresnel numbers," *J. Opt. Soc. Amer. A*, vol. 1, no. 8, pp. 801–808, Aug. 1984.
[27] J. Pu and H. Zhang, "Intensity distribution of Gaussian beams focused by a lens with spherical aberration," *Opt. Commun.*, vol. 151, no. 4–6, pp. 331–338, Jun. 1998.
[28] C. Zapata-Rodriguez and A. Sanchez-Losa, "Three-dimensional field distribution in the focal region of low-Fresnel-number axicons," *J. Opt. Soc. Amer. A*, vol. 23, no. 12, pp. 3016–3026, Dec. 2006.
[29] A. Ishikawa, M. Izutsu, and T. Sueta, "Beam propagation method analysis of optical waveguide lenses," *Appl. Opt.*, vol. 29, no. 34, pp. 5064–5068, Dec. 1990.
[30] A. Rohrbach, "Artifacts resulting from imaging in scattering media: A theoretical prediction," *Opt. Lett.*, vol. 34, no. 19, pp. 3041–3043, Oct. 2009.
[31] F. O. Fahrbach, P. Simon, and A. Rohrbach, "Microscopy with self-reconstructing beams," *Nat. Photon.*, vol. 4, no. 11, pp. 780–785, Nov. 2010.
[32] R. S. Pillai, D. Lorenser, and D. D. Sampson, "Deep-tissue access with confocal fluorescence microendoscopy through hypodermic needles," *Opt. Exp.*, vol. 19, no. 8, pp. 7213–7221, Apr. 2011.
[33] J. C. Jung and M. J. Schnitzer, "Multiphoton endoscopy," *Opt. Lett.*, vol. 28, no. 11, pp. 902–904, Jun. 2003.
[34] P. Hofmann, A. Mafi, C. Jollivet, T. Tiess, N. Peyghambarian, and A. Schulzgen, "Detailed investigation of mode-field adapters utilizing multimode-interference in graded index fibers," *J. Lightw. Technol.*, vol. 30, no. 14, pp. 2289–2298, Jul. 2012.